JOURNAL OF MAGNETIC RESONANCE **126,** 18–29 (1997)
ARTICLE NO. MN971143

A General Approach to Error Estimation and Optimized Experiment Design, Applied to Multislice Imaging of T_1 in Human Brain at 4.1 T

Graeme F. Mason, Wen-Jang Chu, and Hoby P. Hetherington

Department of Medicine, Division of Cardiovascular Disease, Center for Nuclear Imaging Research, 828 8th Court South, University of Alabama at Birmingham, Birmingham, Alabama 35294-4470

Received April 8, 1996; revised February 5, 1997

In this report, a procedure to optimize inversion-recovery times, in order to minimize the uncertainty in the measured T_1 from 2-point multislice images of the human brain at 4.1 T, is discussed. The 2-point, 40-slice measurement employed inversion-recovery delays chosen based on the minimization of noise-based uncertainties. For comparison of the measured T_1 values and uncertainties, 10-point, 3-slice measurements were also acquired. The measured T_1 values using the 2-point method were 814, 1361, and 3386 ms for white matter, gray matter, and cerebral spinal fluid, respectively, in agreement with the respective T_1 values of 817, 1329, and 3320 ms obtained using the 10-point measurement. The 2-point, 40-slice method was used to determine the T_1 in the cortical gray matter, cerebellar gray matter, caudate nucleus, cerebral peduncle, globus pallidus, colliculus, lenticular nucleus, base of the pons, substantia nigra, thalamus, white matter, corpus callosum, and internal capsule.

INTRODUCTION

Experimental optimization of NMR experiments to improve the accuracy of measurement of parameters whose values are known to lie within a given range has previously been based on the use of discrete solutions using operational equations for which the noise was assumed to yield normal distributions of uncertainty in the results, and to be small enough for application of differential calculus (*1–5*). However, in many cases, including some NMR measurements, distributions of uncertainty may be nonnormal, and the noise may not be vanishingly small. In addition, approximations must often be made, or the resulting mathematics become too cumbersome for an analytic solution to be practical, as for the measurement of T_1 with a single inversion-recovery curve that is sampled multiple times (*6–9*).

Previously, it has been demonstrated that at 4.1 T, quantitative imaging of T_1 provides a means by which images can be segmented into components of gray matter (GM), white matter (WM), and cerebral spinal fluid (CSF) (*9*). However, due to the large numbers of points acquired along the recovery curves (ten), the number of slices was restricted to three. The extension of this method to provide quantitative images of T_1 throughout the brain requires a dramatic reduction in the number of time points sampled along a single recovery curve. This in turn places a premium on the optimal choice of inversion-recovery sample times.

In this study, we present a general approach to noise-based error estimation and have used it to minimize the number of sampling points required to obtain multislice quantitative images of T_1 throughout the entire brain, given a known range of T_1 values (815–3500 ms).

METHODS

Statistics

For a function $y = f(\alpha, x)$, where x is the coordinate, y is the measured parameter, and α is the fitted parameter, the uncertainty in α (i.e., σ_{tot}) due to noise in y (i.e., σ_y) can be estimated. The uncertainty in α can often be determined using its sensitivity to variations in y (i.e., $\partial\alpha/\partial y$), where σ_α is given by the error propagation formula

$$\sigma_\alpha = \sqrt{\sum_{i=0}^{n} \left[\left(\frac{\partial \alpha}{\partial y_i} \right)^2 \sigma_{y_i}^2 \right]}.$$

However, application of the error propagation theorem in this instance is only valid when there is a lack of covariance in the data (*10, 11*). Furthermore, the use of $\partial\alpha/\partial y$ assumes that $\partial\alpha$ and ∂y are small, whereas signal-to-noise ratios in many NMR imaging and spectroscopic experiments are large enough to invalidate the assumption. When $\partial\alpha$ and ∂y are not much smaller than α and y, the standard deviation can differ from that estimated using the error propagation theorem. Furthermore, the distributions of uncertainty can also become nonnormal, violating an assumption of the error propagation theorem (*5*). Therefore, while the calculus-based approaches often provide a useful method for error estimation and experimental design, an alternative estimation would be useful for many NMR experiments.

To determine the uncertainty in T_1 for 2- and 10-point measurements for each value of T_1 across the range of expected values, a set of observations was simulated without

1090-7807/97 $25.00

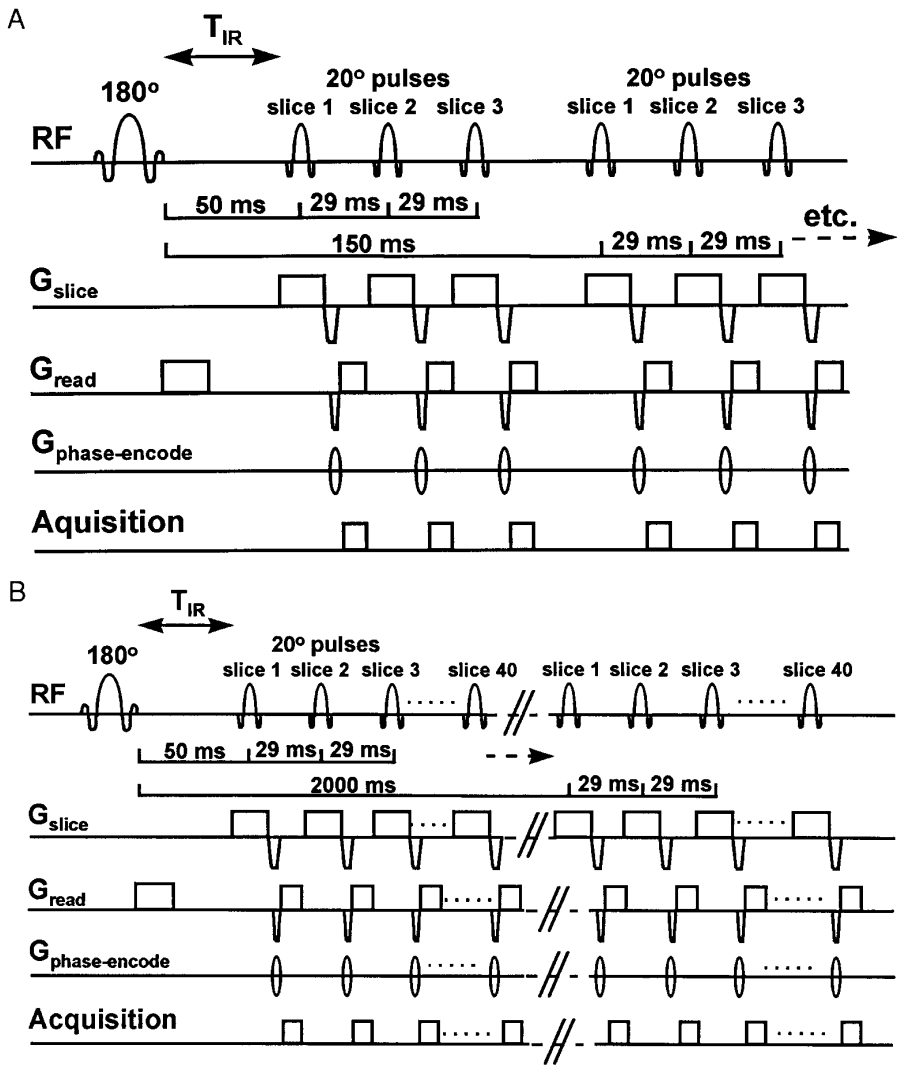

FIG. 1. The sequences used to acquire the 10- and 2-point images. In both cases, a single, nonselective inversion pulse was followed by a series of slice-selective readouts. (A) The 10-point sequence is that shown previously (*9*). An inversion pulse begins the sequence, and 10 triplets of slice-selective acquisitions sample 10 time points for 3 different slices. (B) The 2-point sequence has the same structure, but two sets of 40 slice-selective acquisitions sample 2 time points for 40 different slices.

noise. For the simulations, representative values of T_1 for WM, GM, and CSF [819, 1323, and 3548 ms, respectively; Refs. (*9, 12, 13*)] were used to calculate noiseless recovery curves. Then, 1000 simulated ''noisy'' data sets were generated by adding randomly generated noise to the noiseless data set, using the Gaussian distribution of noise observed in the NMR experiment (*11*). For the present application, the signal-to-noise ratio was 50:1. The 1000 simulated, ''noisy'' data sets were fitted using a simplex algorithm with the T_1 and the initial magnetization as the free parameters, and the standard deviations were calculated.

A variety of combinations of sample times were selected manually and tested in order to find sampling schemes with uncertainties that were adequately small to differentiate the T_1 of GM, WM, and CSF, while retaining the ability to sample large numbers of slices.

NMR Imaging

All data were acquired at 4.1 T, using a ^{1}H volume coil (*14*). A 256 × 256 gradient-echo sagittal scout image was acquired to verify the subject's position. Transverse 256 × 256 gradient-echo scout images were acquired in 3 mm slices for anatomical reference with the T_1 data sets. Ten- and 2-point measurements were acquired from six volunteers.

T_1 images were acquired (*6–9*) using a sequence consisting of a nonselective hyperbolic secant inversion pulse (*15*), followed by a relaxation delay and time series of 3 or 40 20° slice-selective readouts from 3 mm slices separated by 5 mm center-to-center (Fig. 1). For the 2-point measurements, each pair of slice-selective readouts was separated by 1950 ms. The 10-point measurement, which was the gold standard for the uncertainty analysis of the T_1 measurements,

TABLE 1

Relative Uncertainties in T_1 Yielded by Various Pairs of Inversion-Recovery Sample Times, When the Signal-to-Noise Ratio of White Matter at T_{IR} = 50 ms Is 50:1, As Was the Case in the Present Study

T_{IR} spacing (ms)	T_{IR} (ms)	σ_{T_1} (% of T_1)			T_{IR} (ms)	σ_{T_1} (% of T_1)			T_{IR} (ms)	σ_{T_1} (% of T_1)		
		WM	GM	CSF		WM	GM	CSF		WM	GM	CSF
150	50, 200	6.86	14.10	100.00	634, 784	4.21	5.71	100.00	1218, 1368	19.50	15.22	100.00
350	50, 400	3.31	5.90	36.24	634, 984	3.19	2.72	29.38	1218, 1568	9.40	7.77	10.12
550	50, 600	2.69	4.17	22.33	634, 1184	2.94	2.64	17.02	1218, 1768	6.70	5.96	8.38
750	50, 800	2.65	3.58	16.67	634, 1384	2.82	2.76	12.56	1218, 1968	5.45	5.12	8.60
950	50, 1000	2.86	3.42	13.84	634, 1584	2.75	2.89	10.66	1218, 2168	4.74	4.64	8.99
1150	50, 1200	3.19	3.50	12.36	634, 1784	2.70	3.03	9.88	1218, 2368	4.27	4.32	9.35
1350	50, 1400	3.63	3.72	11.58	634, 1984	2.66	3.14	9.68	1218, 2568	3.96	4.10	9.68
1550	50, 1600	4.18	4.05	11.31	634, 2184	2.65	3.26	9.81	1218, 2768	3.72	3.92	9.98
1750	50, 1800	4.84	4.50	11.41	634, 2384	2.63	3.36	10.14	1218, 2968	3.57	3.79	10.25
1950	**50, 2000**	**5.63**	**5.07**	**11.82**	**634, 2584**	**2.61**	**3.45**	**10.59**	**1218, 3168**	**3.44**	**3.67**	**10.48**
2150	50, 2200	6.58	5.78	12.50	634, 2784	2.60	3.54	11.14	1218, 3368	3.35	3.58	10.70
2350	50, 2400	7.70	6.68	13.46	634, 2984	2.60	3.61	11.75	1218, 3568	3.27	3.51	10.90
2550	50, 2600	9.02	7.82	14.74	634, 3184	2.60	3.69	12.42	1218, 3768	3.22	3.44	11.07
2750	50, 2800	10.55	9.27	16.35	634, 3384	2.59	3.75	13.14	1218, 3968	3.17	3.38	11.21
10-pt		1.56	2.06	7.75	—				—			

Note. The boldface row, spacing of 1950 ms, was chosen because the wide spacing of the points allowed up to 60 slices to be acquired, while maintaining fairly uniform compromises of uncertainty among the three tissue types over many slices. The last line, recorded as ''10-pt'' under the T_{IR} spacing column, shows the error obtained in a single slice, using the 10 T_{IR} values of 50, 150, 250, 350, 450, 600, 800, 1000, 1250, and 1500 ms.

employed sample times of 50, 150, 250, 350, 450, 600, 800, 1000, 1250, and 1500 ms for the first slice, with increments of 29.2 ms per slice. All slices were 3 mm thick and acquired with a 5 mm center-to-center separation to permit coverage of the entire brain.

T_1 Image Processing

The images were reconstructed using PV-WAVE (Precision Visuals, Inc., Boulder, Colorado) and phase corrected to provide real images. An intensity threshold determined by the user was applied to the real image to eliminate regions from outside the head from further analysis. The T_1 from each pixel was determined by fitting the time course of the magnetization using a simplex algorithm with the T_1 and the initial magnetization as the free parameters. The results of the iteration were stored as 256 × 256 images of T_1.

Evaluation of T_1

Due to subject motion between scans, a direct pixel-by-pixel comparison of all acquired locations was not feasible. Therefore, to compare the calculated values of the T_1 of WM, GM, and CSF from the 10- and 2-point image sets, voxels that consisted primarily of WM, GM, or CSF were selected. Individual pixels were assigned as WM, GM, or CSF, determined from images with the highest contrast acquired from each series, using image contrast and anatomic location as criteria for assignment. The contrast depended on the number and values of inversion-recovery sampling

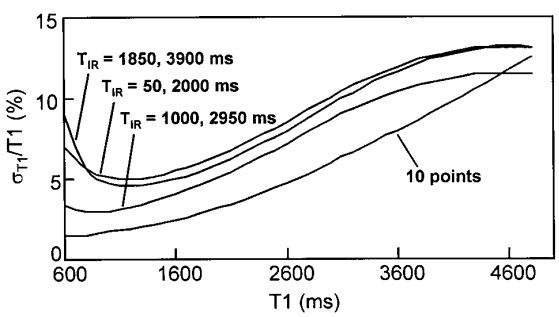

FIG. 2. The predicted effects of 2-point sampling schemes with a 1950 ms gap on the value of σ_{T_1} as a function of T_1. (Middle) σ_{T_1}/T_1 predicted for T_{IR} = 50, 2000 ms. (Bottom) σ_{T_1}/T_1 predicted for T_{IR} = 1000, 2950 ms. (Top) σ_{T_1}/T_1 predicted for T_{IR} = 2000, 2950 ms.

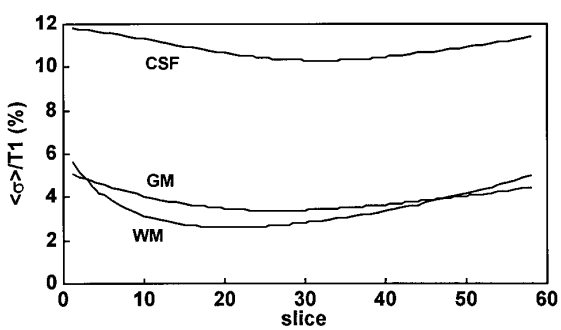

FIG. 3. The uncertainty of T_1 predicted for WM, GM, and CSF over 60 slices. Uncertainties are expressed as a percentage of the T_1.

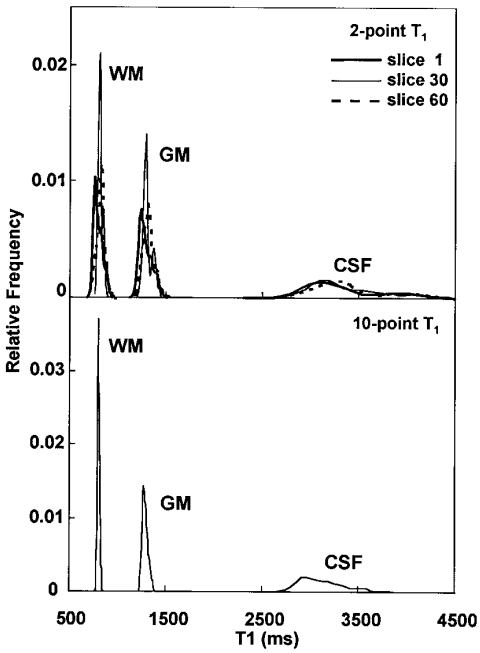

FIG. 4. Predicted uncertainty distributions determined from 1000 iterative noise calculations, assuming equal areas of tissue content. (Top) The 2-point measurements for the 1st, 30th, and 60th slices. (Bottom) The 10-point measurements.

times used for each set. For the 10- and 2-point methods, respectively, the 9th time point and 1st time points showed the highest contrast among tissue types, and an average total of 29 WM, 30 GM, and 21 CSF voxels were chosen for each subject. For the 2-point T_1 image series, over 35 of the slices contained brain tissue, but only the center 17–19 slices contained pure WM and GM in volumes large enough for voxels to be chosen that would minimize partial volume effects. While sulcal CSF was visible in all of the slices that contained brain tissue, only the 5–6 slices that contained significant ventricular volumes were measured, in order to minimize partial volume effects. Altogether, 100 slices were examined for WM, 92 for GM, and 32 for CSF in the 2-point measurements. In 88% of the slices, 9–10 voxels each of predominantly WM and GM were identified, and in the rest of the slices 5–8 voxels were measured. In the ventricular slices, 5–10 voxels of CSF were chosen. The locations of the voxels were used to obtain T_1 values from the fitted T_1 images, and the average T_1 of each tissue type was recorded for each slice. The mean T_1 values and standard deviations of WM, GM, and CSF for each subject were calculated from the T_1 values in all of the sampled slices for each subject.

Measurements of T_1 in Brain Structures

To evaluate regional and structural differences in the T_1 of WM and GM, an average of 509 voxels was chosen for each subject from the two-point T_1 maps representing the cortical gray matter, cerebellar gray matter, caudate nucleus, cerebral peduncle, globus pallidus, colliculus, lenticular nucleus, base of the pons, substantia nigra, the thalamus, white matter, corpus callosum, and the internal capsule. To minimize correlation among selected pixels due to the point-spread function, only nonadjacent voxels were selected. A mean T_1 value for each structure was recorded for each volunteer, and the six means were used to calculate an average and standard deviation for the group.

Image Segmentation

Each pixel in the T_1 image was assigned to one of four bins, corresponding to GM, WM, CSF, or extracerebral volume, based on representative ranges of values measured for T_1 in the specific tissue types. The upper and lower limits for T_1 ranges in each bin were chosen as the midpoints between the means of WM/GM and GM/CSF, with a lower limit of 600 ms used as the cutoff for WM (*9*).

RESULTS

Experiment Design

Previously, we reported the use of a three-slice, 10-time-point measurement to provide quantitative images of T_1 in the human brain for image segmentation. However, in order to image the entire head, it was necessary to increase the number of slices considerably. The increase was achieved by limiting the number of inversion-recovery points to 2 and optimizing the sequence to measure T_1 over the broad range of T_1 values known for brain water at 4.1 T. The T_1 values of WM, GM, and CSF at 4.1 T have previously been reported to be 819, 1323, and 3548 ms, respectively (*9, 12, 13*).

The uncertainty σ_{T_1} of the T_1 of WM, GM, and CSF was estimated for various combinations of spacings of T_{IR} values (Table 1), chosen manually. The analysis indicated that spreading the sample points farther apart increases the range of values of T_1 that are measured with good precision, in agreement with earlier findings (*3, 16*). For the acquisition of many slices over a broad range of T_1 values, some compromise was required. For example, the uncertainty for slices that are acquired early in the recovery curve (that is, for images acquired with the first sample time at $T_{IR} = 50$ ms) was slightly better when smaller T_{IR} spacing was used, while slices acquired later in the recovery curve (e.g., $T_{IR} = 1218$ ms) had better precision with broader T_{IR} spacing. A spacing of 1950 ms was chosen for the separation of the two T_{IR} values, because the 1950 ms spacing had good accuracy for all slices and allowed enough time for the acquisition of as many as 60 slices.

Displayed in Fig. 2 is a plot of σ_{T_1}/T_1 as a function of the true T_1, for three 2-point measurements and the 10-point measurement described previously. As can be seen, for a gap of 1950 ms, σ_{T_1}/T_1 ranges from 3 to 14% over a range

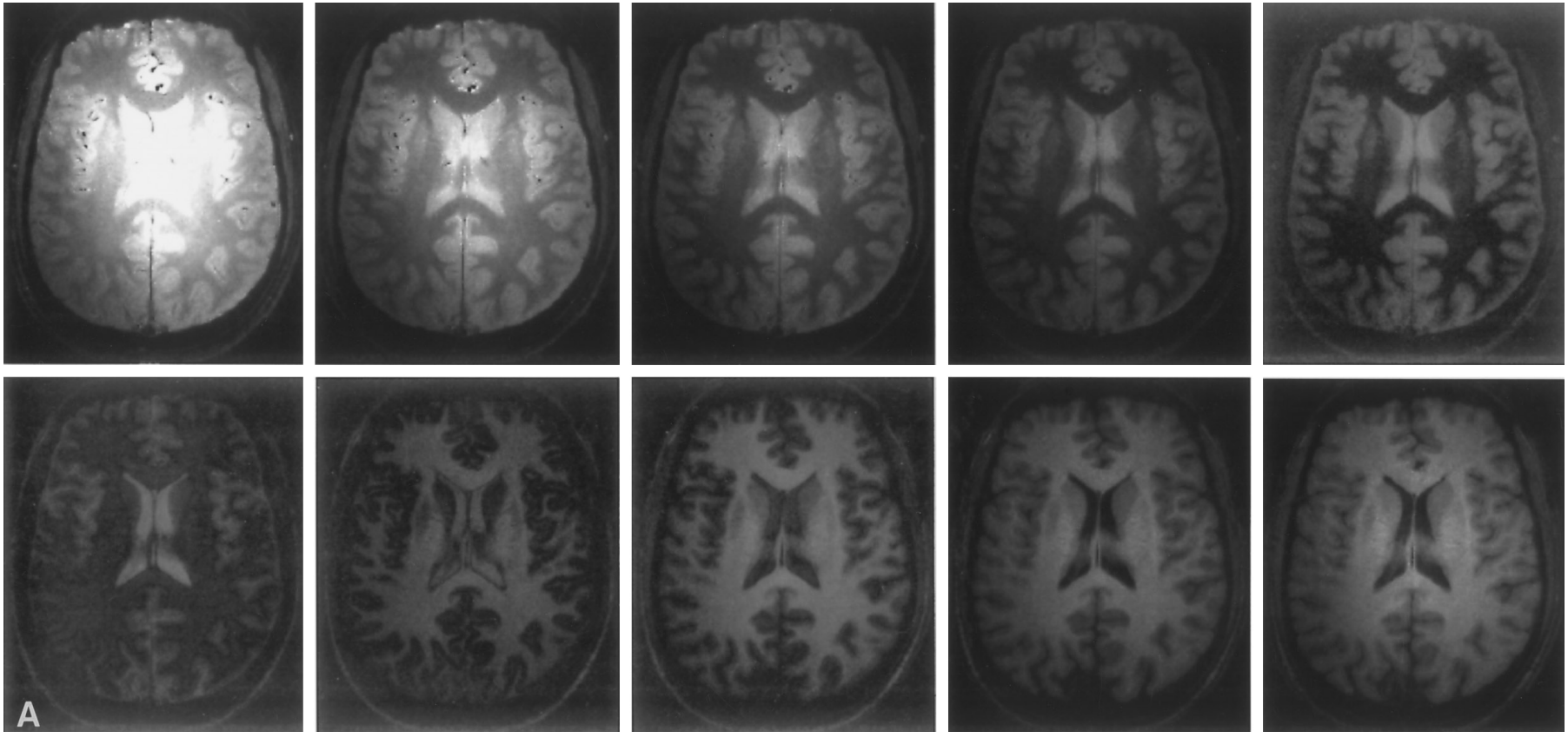
A

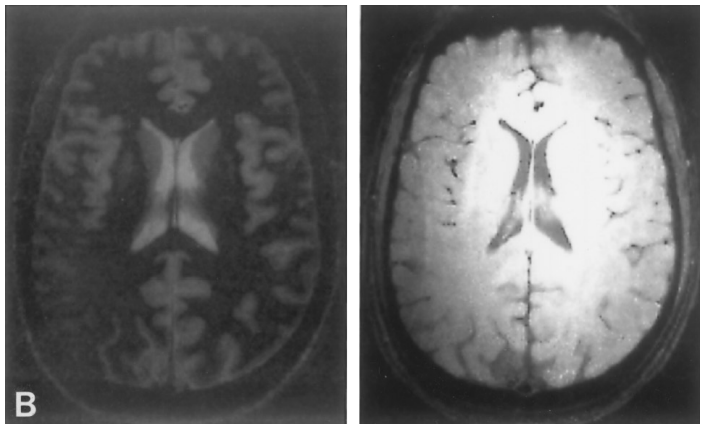

FIG. 5. Image time courses from the T_1 measurement. (A) Ten-point image series. (B) Two-point image series.

of 600 to 5000 ms. For the 10-point measurement, σ_{T_1}/T_1 ranges from 2 to 13%. Employing a 29.2 ms recycle time between slices and a gap of 1950 ms permitted the acquisition of nearly 60 3 mm slices. However, 40 axial slices with 5 mm center-to-center separation were found to be more than adequate to cover the brain in the cranial to caudal direction.

Figure 3 shows the predicted effects of the two-point measurement on the noise-induced uncertainty in T_1 for WM, GM, and CSF as a function of slice number. For this simulation, the T_1 values of WM, GM, and CSF were assumed to be 819, 1323, and 3548 ms, respectively (*9*). The sample times for slice 1 were 50 and 2000 ms, for slice 2 were 79.2 and 2029.2 ms, for slice 3 were 108.4 and 2058.4 ms, and so on. Because the sample times differed for each slice, the uncertainty is a function of sample time (see Fig. 2) and, therefore, slice number. The uncertainty varied the least for CSF, because the slice-dependent changes in sample times represented a smaller fraction of the very long T_1 of CSF, relative to the much shorter T_1 values of WM and GM. While the precision of the T_1 of CSF is more than adequate to use it as a basis for distinguishing it from WM and GM, its estimated uncertainty is larger than those of GM and WM, due to the reduced accuracy of the measurement at high T_1 values (see Fig. 3).

Figure 4 displays the predicted uncertainty distributions for the 10- and 2-point measurements for WM, GM, and CSF as a function of the calculated T_1. Because each slice has a different combination of sample times, the distributions differ as functions of the slice number. For some slices, the distributions are normal, while for other slices the uncertainties are skewed toward higher values or are even bimodal. The skewing and bimodal behavior arise due to unequal and asymmetric influences on the fitted parameters at the two data points. Therefore, as was discussed earlier, the noise in the present study cannot be assumed to yield normal distributions of uncertainty, as would be required for accurate application of the error propagation theorem.

Ten- and Two-Point T_1 Images

Representative image time courses from the 2- and 10-point image T_1 measurements are displayed in Figs. 5A and 5B. Figures 6A and 6B show sample image pixel time courses for WM, GM, and CSF in the two image sets, with the least-squares fits superimposed. The nonnegligible effect of the 20° sampling pulse is quite apparent in the initial readouts of CSF and the final samples of WM and GM. Figure 6C shows the T_1 images resulting from the two time series of Fig. 5. In the T_1 images, the ventricles and sulci are brightest, because CSF has the highest T_1 value. The cortical and subcortical GM have the middle level of brightness due to their intermediate values of T_1, while WM, with the shortest T_1, is darker. In order to evaluate the distributions of T_1, histograms for two slices imaged with 10- and 2-point methods are shown in Fig. 7. Even so, the overlap of T_1 is greater than would be expected based on noise alone (see Fig. 4) and most likely results from partial volume effects arising from through-plane variations in the 3 mm slices and the in-slice variations of border regions between WM and GM.

The mean and standard deviations of T_1 for WM, GM, and CSF in each slice are shown in Figs. 8 and 9, respectively. Because the shape and size of each volunteer's head was different, different ranges of slices were available to measure the T_1 of each tissue type. The T_1 shows a slight upward trend as a function of slice number, which is in agreement with the predictions illustrated in Fig. 4. In contrast, the standard deviation showed no evidence of a trend, which is a reflection both of the size of the change expected from Fig. 4 and of the fact that the measured variability results primarily from the partial volume effects demonstrated by the histograms in Fig. 7.

T_1 of Brain Structures

Presented in Table 2 are the regional values of T_1 from a variety of structures, as determined from the two-point

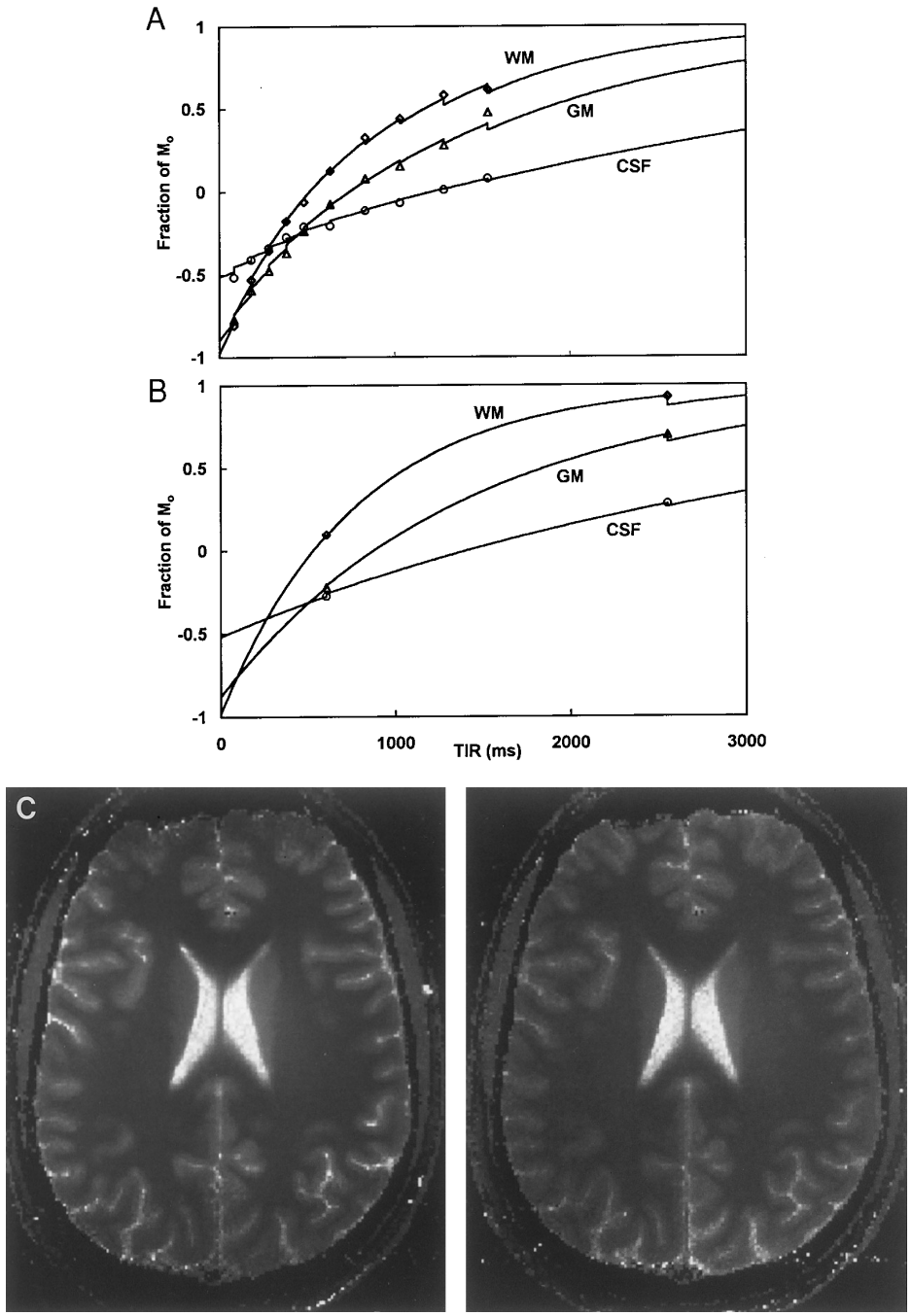

FIG. 6. Time courses of image pixel intensities for the image series in Fig. 5, with least-squares fits superimposed. Fits are shown for (A) 10-point T_1 imaging and (B) 2-point T_1 imaging. The exponential behavior of the inversion recovery curves is interrupted periodically by the 20° excitation used to sample the curve, and the effect of this behavior was included in the fit. (C) Fitted T_1 images are also shown for the 10-point and 2-point series of Fig. 5.

measurements. For WM structures such as frontal, parietal, occipital, and temporal WM, the T_1 values ranged from 787 ± 47 to 856 ± 46 ms. For cortical GM in the frontal, parietal, occipital, and temporal regions, the T_1 ranged from 1228 ± 64 to 1352 ± 98 ms. Subcortical structures of GM, such as the lenticular nucleus, thalamus, putamen, globus pallidus, and caudate nucleus showed similar but shorter T_1 values of 1174 ± 62, 1214 ± 72, 1271 ± 81, 1124 ± 99, and 1354 ± 84 ms, respectively. Specifically, differences of the T_1 values measured from the basal ganglia, the caudate nucleus, globus pallidus, and putamen help to resolve these regions in high-resolution T_1-weighed images (*13*).

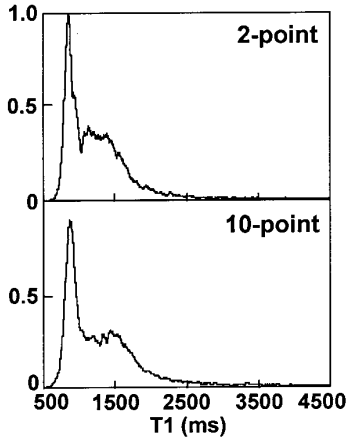

FIG. 7. Histograms of T_1 distributions for (top) a 2-point measurement and (bottom) a 10-point measurement. The estimated uncertainty distributions (Fig. 4) are narrow enough to achieve separation of tissue types, whereas in the actual image, partial volume effects cause significant overlap.

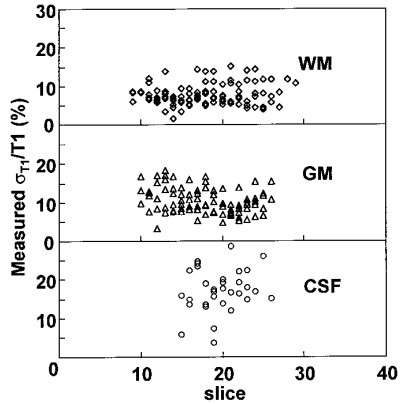

FIG. 9. The measured uncertainties in T_1 as a function of slice number. The slice standard deviations measured for 2-point measurements of WM, GM, and CSF are presented relative to the T_1 of the respective tissue types.

DISCUSSION

Image Segmentation

Although regional and structural variations in T_1 values exist, there appears to be sufficient grouping of the values to segment the primary tracts of GM, WM, and CSF from each other using simple numerical bins. In the 10-point images, the tissue-type bin limits were 1087 and 2374 ms for GM/WM and GM/CSF, respectively. In the 2-point images, the bin limits for GM/WM and GM/CSF were 1073 and 2324 ms, respectively. Figure 10A shows the quantitative image of T_1, with 3 mm slice thickness and 5 mm center-to-center slice separation, calculated from the 2-point, 40-slice acquisition for one subject. Only those slices that contained brain tissue are shown. In order to obtain segmented images of tissue type, each pixel in the slices of Fig. 10A was assigned to one of four gray scale levels corresponding to WM, GM, CSF, or extracranial tissue, based on the value of T_1 in each pixel. Figure 10B shows the resulting binned, segmented images.

The reported standard deviations of ~5% for WM and GM for the group (Table 3) are consistent with the predicted values of σ_{T_1}/T_1. However, standard deviations of T_1 for individual slices in the two-point measurement are higher (5–10%). Some portion of the standard deviations in each slice probably results from partial volume effects, but some variability could result from B_1 inhomogeneity. B_1 inhomogeneity can affect the sequence either by reducing the inversion efficiency or by altering the excitation angle. Because the hyperbolic secant used for the inversion is B_1 insensitive beyond a threshold level of B_1 (*15*), the B_1 sensitivity arises primarily from variability in the 20° excitation pulse.

The T_1 was calculated assuming an excitation angle of 20°. In order to quantify potential errors due to B_1 inhomogeneity, the pixel time courses were simulated assuming excitation angles of 18° and 22° (±10% of the calibrated B_1), which was a factor of two greater than the homogeneity of the RF coil (*14*). For the 10-point measurements, the pre-

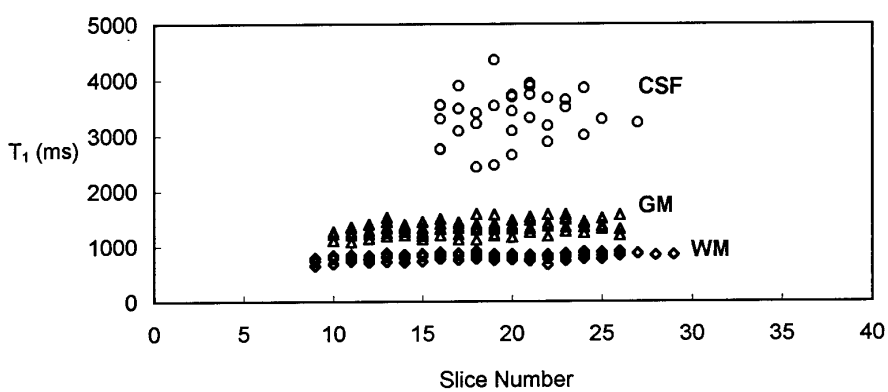

FIG. 8. T_1 values measured with two points over the range of sampled slices for all six volunteers. The slight upward trends in the T_1 of WM and GM, as a function of slice number, agrees with the predictions shown in Fig. 4.

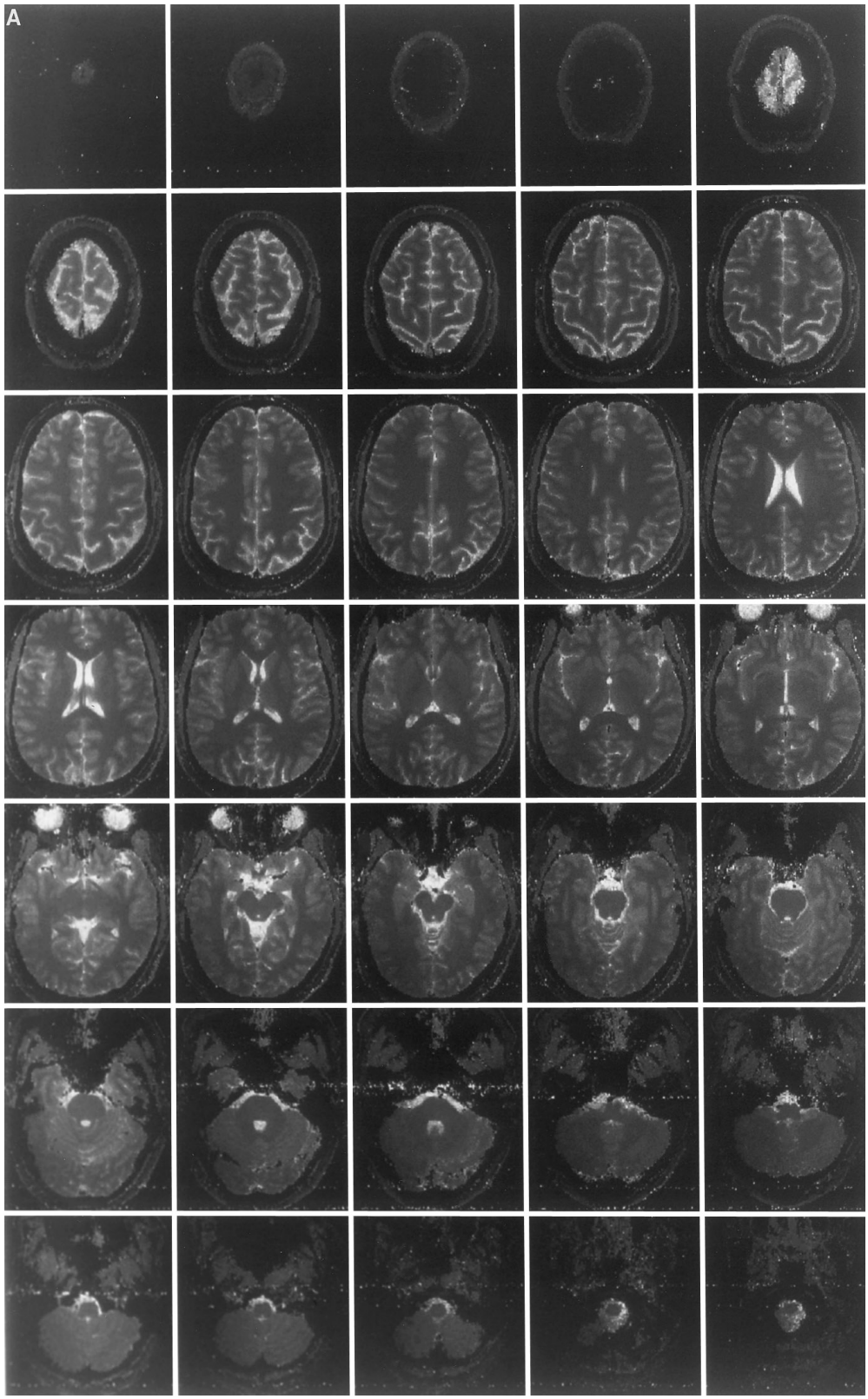

FIG. 10. Results of a 40-slice acquisition, showing only the 35 slices that contained tissue. (A) Quantitative T_1 images from the same subject as in Figs. 5 and 6. The T_1 values in the images were assigned to tissue types based on the bin limits designated as the midpoints of the measured means of T_1 of WM/GM and GM/CSF to obtain (B) four-level segmented images of gray matter, white matter, CSF, and extracranial pixels.

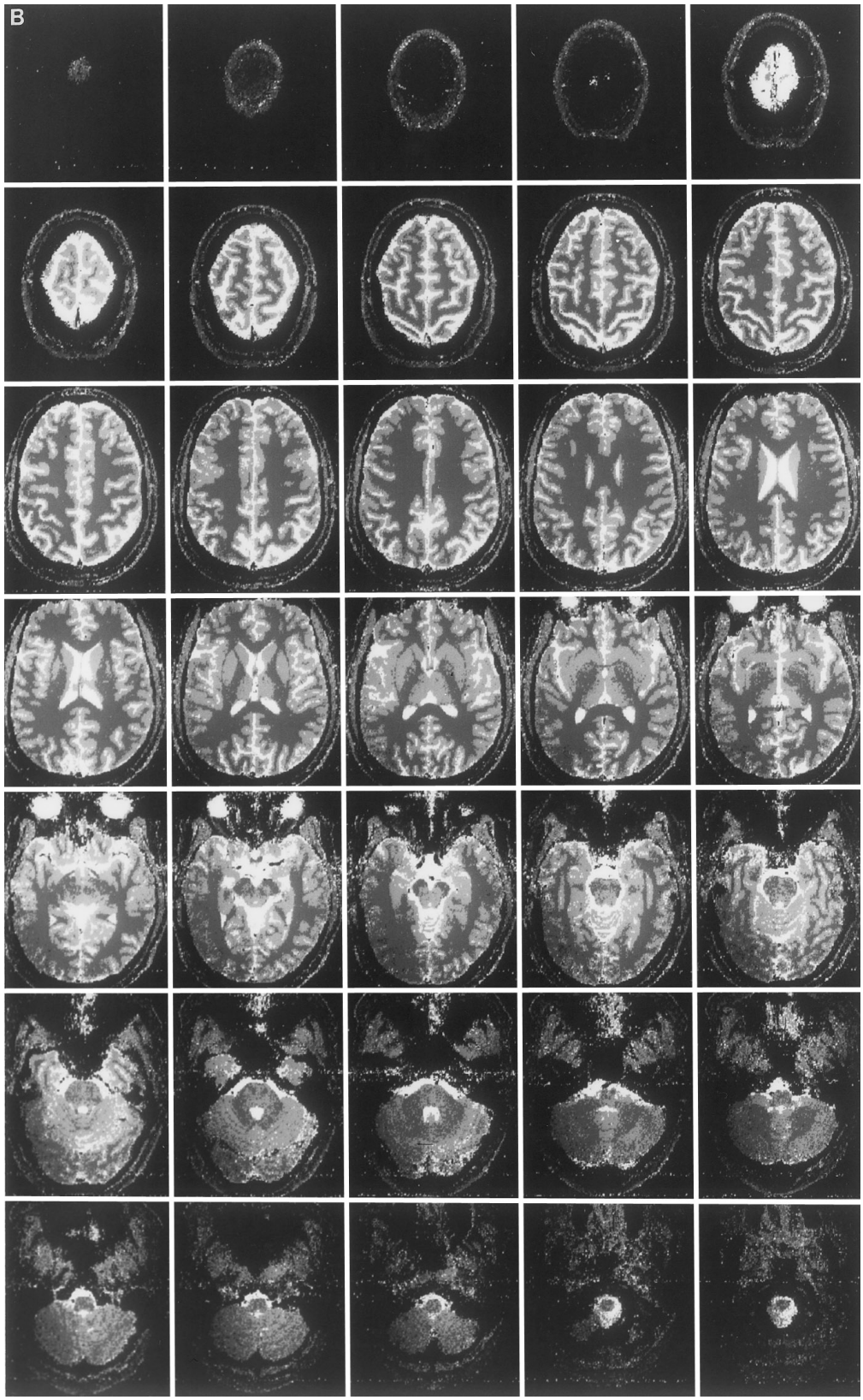

FIG. 10—*Continued*

dicted errors due to B_1 inhomogeneity were approximately ±2% for WM, ±4% for GM, and ±17% for CSF. The estimated errors for the 2-point measurement were significantly smaller, being less than ±1% for WM and GM and ±2% for CSF. The difference in the B_1 sensitivity of the 2- and 10-point measurements of T_1 results from the occurrence of only 2 excitation pulses, instead of 10. These B_1 sensitivity calculations show that B_1 inhomogeneity is not expected to contribute significantly to the variability in T_1.

A more significant contribution to uncertainty is expected to be partial volume effects. In some slices (e.g., those immediately above the corpus callosum), sulci are oriented more longitudinally than in others and so provide purer GM in the through-slice direction than others. Other orientations of sulci will yield more through-slice contamination by WM or CSF, causing the observed T_1 to be shorter or longer, respectively. This may in part explain the higher values recorded for hippocampal T_1, due to the highly complex anatomy and the extent of CSF surrounding the structure.

The images of Fig. 6 and Fig. 10 show that images of T_1 can be made of brain water ranging from 819 to 3548 ms at a field strength of 4.1 T. The two-point, widely spaced samples yielded an effective measurement protocol for multislice imaging of T_1 and tissue type. The general approach that was used allows the consideration of nonnormal distributions of uncertainties, whether for measurement of T_1 or other parameters. The present application shows that the approach is valid for nonnegligible noise levels, which are a common feature of many NMR experiments, including anatomic and spectroscopic imaging and single-voxel spectroscopy.

TABLE 2
T_1 Values of Brain Structures Measured in the 40-Slice Two-Point T_1 Images from Six Subjects

Structure	T_1 (ms)	Voxels/ subject
Frontal cortical GM	1311 ± 66	60
Parietal cortical GM	1228 ± 64	43
Occipital cortical GM	1236 ± 69	42
Temporal cortical GM	1352 ± 98	19
Hippocampus	1413 ± 128	11
Cerebellar GM	1353 ± 132	4
Frontal WM	831 ± 37	59
Parietal WM	827 ± 38	43
Occipital WM	787 ± 47	45
Temporal WM	856 ± 46	15
Cerebellar WM	927 ± 90	6
Corpus callosum	835 ± 32	24
Cerebral peduncle	940 ± 56	10
Cerebellar peduncle	1040 ± 93	4
Colliculus	1098 ± 95	6
Decussation of superior cerebellar peduncle	1067 ± 91	6
Internal capsule, anterior limb	965 ± 99	10
Internal capsule, genu	886 ± 49	5
Internal capsule, posterior limb	908 ± 48	9
Base of pons	1007 ± 64	7
Substantia nigra	1120 ± 115	8
Caudate nucleus	1354 ± 84	27
Thalamus	1214 ± 72	17
Lenticular nucleus	1174 ± 62	6
Putamen	1271 ± 81	13
Globus pallidus	1124 ± 99	10

Note. T_1 values are given as mean ± standard deviation.

TABLE 3
T_1 Values of White Matter, Gray Matter, and Cerebral Spinal Fluid Measured in Images of the Brains of Six Healthy Human Subjects, Using Either 10- or 2-Point Inversion-Recovery Sequences

	T_1 (ms)		
	WM	GM	CSF
10 points	814 ± 58	1361 ± 107	3386 ± 460
2 points	817 ± 43	1329 ± 104	3320 ± 325

Note. The values differ insignificantly ($p > 0.1$).

In the present case, the goal was to use as few data points as possible in order to measure a broad range of T_1 over a large volume of the brain. A potential application for other experiments would be to limit the number of data points so as to improve the measurement accuracy with more signal averages at each sampling point.

It has been shown previously that for a two-parameter fit such as the present application (T_1 and initial magnetization), the minimum number of sample points is two (*17*), and that the those two points should always be a subset of a measurement with a larger number of samples. While the first requirement of two parameters and two samples holds true, the second behavior was not observed in the present case. For the T_1 imaging sequence, the occurrence of each 20° excitation pulse creates a situation in which the act of obtaining one observation alters the observed response in subsequent observations.

The present application was used to design measurements of T_1, given prior knowledge of the potential range of the T_1 values. However, the final design was chosen so as to measure a broad range of T_1 values (800–3500 ms), including not only the specific T_1 values of WM, GM, and CSF, but other T_1 values that might appear in disease. For shorter or longer T_1 values, other numbers or spacing of the sampling points could be used to accommodate the new values.

In this study, a manual, subjective choice of inversion-recovery sample spacing was obtained after inspection of the distributions of uncertainties for different sampling times. It may be possible to obtain a more objective approach with an iterated, least-squares minimization of the error across all slices to be studied.

In summary, for parameters that lie within a known range of possibilities, it is possible in a general way to design an

experimental protocol that allows efficient measurement of those parameters, including the effects of noise and nonnormal distributions of uncertainties.

ACKNOWLEDGMENTS

This work was supported by the National Center for Research Resources, National Institutes of Health (Grant RR-07723). Thanks also to Dr. Yantian Zhang for bringing several important references to the authors' attention.

REFERENCES

1. G. H. Weiss and J. A. Ferretti, *Prog. NMR Spectrosc.* **20,** 317 (1988).
2. H. Taitelbaum, J. A. Ferretti, R. G. S. Spencer, and G. H. Weiss, *J. Magn. Reson. A* **105,** 59 (1993).
3. P. A. Bottomley and R. Ouwerkerk, *J. Magn. Reson. B* **104,** 159 (1993).
4. P. A. Bottomley, H. C. Charles, P. B. Roemer, D. Flamig, H. Engeseth, W. A. Edelstein, and O. M. Mueller, *Magn. Reson. Med.* **7,** 319 (1988).
5. G. F. Mason, G. M. Pohost, and H. P. Hetherington, *J. Magn. Reson. B* **107,** 68 (1995).
6. D. C. Look and D. R. Locker, *Rev. Sci. Instrum.* **41,** 250 (1970).
7. A. Haase, *Magn. Reson. Med.* **13,** 77 (1990).
8. I. Kay and R. M. Henkleman, *Magn. Reson. Med.* **22,** 414 (1991).
9. H. P. Hetherington, J. W. Pan, G. F. Mason, D. B. Twieg, D. Adams, and G. M. Pohost, *Magn. Reson. Med.* **36,** 21 (1996).
10. G. E. P. Box, W. G. Hunter, and J. S. Hunter, ''Statistic for Experimenters: An Introduction to Design, Data Analysis, and Model Building,'' Wiley, New York, 1978.
11. P. R. Bevington, and D. K. Robinson, ''Data Reduction and Error Analysis for the Physical Sciences,'' McGraw-Hill, New York, 1992.
12. K. Ugurbil, M. Garwood, J. Ellermann, K. Hendrich, R. Hinke, X. Hu, S.-G. Kim, R. Menon, H. Merkle, S. Ogawa, and R. Salmi, *Magn. Reson. Q.* **9,** 259 (1993).
13. J. W. Pan, J. T. Vaughan, R. I. Kuzniecky, G. M. Pohost, and H. P. Hetherington, *Magn. Reson. Imaging* **13,** 915 (1995).
14. J. T. Vaughan, H. P. Hetherington, J. O. Out, and G. M. Pohost, *Magn. Reson. Med.* **32,** 206 (1994).
15. M. S. Silver, R. I. Joseph, C. N. Chen, V. J. Sarky, and D. I. Hoult, *Nature (London)* **310,** 681 (1984).
16. H. Taitelbaum, J. A. Ferretti, R. G. S. Spencer, and G. H. Weiss, *J. Magn. Reson. A* **109,** 166 (1994).
17. M. J. Box, *Technometrics* **1,** 569 (1970).